

Defect design in ferroelectrics – new insights on agglomeration

Sheng-Han Teng, Anna Grünebohm

^a*Interdisciplinary Centre for Advanced Materials Simulation (ICAMS) and
Center for Interface-Dominated High Performance Materials (ZGH), Ruhr-University
Bochum, Univeristätstr. 150, Bochum, 44780, Germany*

Abstract

Functional properties of ferroelectrics and their change with time depend crucially on the defect structure. In particular, point defects and bias fields induced by defect dipoles modify the field hysteresis and play an important role in fatigue and aging. However, a full understanding on how order, agglomeration and strength of defect dipoles affect phase stability and functional properties is still lacking. To close these gaps in knowledge, we screen these parameters by *ab initio* based molecular dynamics simulations with the effective Hamiltonian method for the prototypical ferroelectric material (Ba,Sr)TiO₃. Our findings suggest that the *active surface area* of the defects, rather than the defect concentration is the decisive factor. For a fixed defect concentration, clustering reduces the *active surface area* and thus the defect-induced changes of phase stability and field hysteresis. Particularly planar agglomerates of defects appear as promising route for the material design as their impact on the field hysteresis can be controlled by the field direction and their impact on the phase stability shows a cross-over with the strength of the defect dipoles. For this agglomeration, we furthermore find that pinched field hysteresis, which is beneficial, e.g. for energy storage, can be achieved for a wide range of defect dipole strengths and thus is not too sensitive to the choice of dopants.

Keywords: Ferroelectric, Phase diagrams, Field hysteresis, Point defects, Molecular Dynamics Simulations

1. Introduction

The exceptional dielectric, caloric, and piezoelectric functional responses of ferroelectric perovskites in the vicinity of structural phase transitions, as well as their adjustable field hysteresis in the ferroic phases, make these materials important for a wide range of applications [1, 2] including energy storage and electronic devices. [3, 4] Adjusting transition temperatures and functional properties is commonly done by chemical substitution.[5, 6, 7] Thereby, one has to distinguish between isovalent substitution, e.g. substitution of Ba in BaTiO_3 by Sr or Ca ($\text{Sr}_{\text{Ba}}^\times$, $\text{Ca}_{\text{Ba}}^\times$), or Ti by Zr ($\text{Zr}_{\text{Ti}}^\times$), and aliovalent substitution, e.g. substitution of Ti by Fe or Nb (Fe'_{Ti} , Nb_{Ti}). In the former case, the substituents introduce local distortions and commonly reduce transition temperatures. [7, 8] Although changes of the local polarization [8] and even non-polar cells may occur,[9, 10, 6] the dynamics of the local switching are not changed significantly for small defect concentrations, as all dipoles switch by ionic displacements happening on the ps-scale.[11, 12] In the latter case, depending on the type and distribution of the dopant and the thermal treatment of the system, changes of transition temperatures and internal bias fields with shifting and pinching of hysteresis loops have been reported. [13, 14, 15] As internal restoring forces and pinched hystereses are beneficial for energy storage [3] as well as large reversible piezoelectric[16] and electrocaloric responses, [17, 18] this field arose considerable attention. It is accepted that these observations are related to charge compensation by vacancies and the formation of defect complexes with local dipole moments, such as $(\text{Fe}'_{\text{Ti}}-\text{V}\ddot{\text{O}})^\cdot$ and $(\text{Mn}''_{\text{Ti}}-\text{V}\ddot{\text{O}})^\times$. [16, 19] Switching of these defect complexes requires slow ion migration which may take more than 10^7 s at room temperature.[19, 20, 21] Thus these defects align with the surrounding polarization during aging and later act as restoring forces on domain and phase structure. It is furthermore accepted that changes of the functional properties with time, e.g., functional fatigue, are related to ion migration and redistribution of defects. [22, 13] In experimental samples, the distribution of defects depends on processing, thermal treatment, field-loading and internal and external boundaries, e.g. electrodes, grains, or dislocations [23, 13]. For example, the uniform random distribution after ion-bombardment, [24] planar arrays of oxygen vacancies in reduced atmosphere,[25] defect planes in a severely fatigued sample,[26] clustering of oxygen vacancies,[27] and agglomeration of defects at dislocation lines [28] have been reported.

To tap the full potential of defect-engineering and to improve the un-

derstanding of functional fatigue, a microscopic understanding is mandatory. Since most microscopic modeling so far focuses on the alignment of single defect dipoles, even after decades of research, this understanding is still incomplete. In the present study, we use an *ab initio* derived effective Hamiltonian to screen the impact of defect distribution on ferroelectric phase diagrams and field hystereses in BaTiO₃ solid solutions. Thereby we focus on point defects without local polarization and defect dipoles which re-orient orders of magnitude slower than the switching by Ti off-centering and can thus be approximated by fixed dipoles,[19, 21] see Fig.1. We show that although the impact of the defects on phase transition and field hysteresis depends on defect strength and concentration, the distribution and agglomeration of defects play an even larger role.

2. Methods

2.1. Molecular dynamics simulations

We use the effective Hamiltonian from Ref. 29, which is parameterized based on first-principles calculations for the solid solution of (Ba,Sr)TiO₃:[30]

$$\begin{aligned}
H^{eff} = & \frac{M_{dipole}^*}{2} \sum_{\mathbf{R},i} \dot{u}_i^2(\mathbf{R}) \\
& + V^{self}(\{\mathbf{u}\}) + V^{dpl}(\{\mathbf{u}\}) + V^{short}(\{\mathbf{u}\}) \\
& + V^{elas,homo}(\eta_\alpha) + V^{elas,inho}(\{\mathbf{w}\}) \\
& + V^{coup,homo}(\{\mathbf{u}\}, \eta_\alpha) + V^{coup,inho}(\{\mathbf{u}\}, \{\mathbf{w}\}) \\
& + V^{mod,inho}(\{\mathbf{w}\}, \{s\}) - Z^* \sum_{\mathbf{R},i} \mathcal{E} \cdot u_i(\mathbf{R}), \tag{1}
\end{aligned}$$

where $\{\mathbf{u}\}$, $\{\mathbf{w}\}$, η_α ($\alpha = 1, \dots, 6$), $\{s\}$, Z^* and \mathcal{E} are local soft mode vectors in Cartesian coordinates i ($= x, y, z$), local acoustic displacement vectors, the tensor of homogenous strain, the relative number of Ba and Sr atoms in each unit cell (u.c.), the Born effective charge associated with the soft mode, and an external electrical field, respectively. The local mode gives the local polarization as $\mathbf{P} = eZ^*\mathbf{u}/a^3$ where e is the elementary charge and a is the lattice constant. Without loss of generality, we study Ba_{0.7}Sr_{0.3}TiO₃ with its Curie temperature close to room temperature using a random distribution of Sr in combination with the chemical modulation $V^{mod,inho}$ which depends on the Sr concentration in the unit cell and a pressure correction of -1.2 GPa,

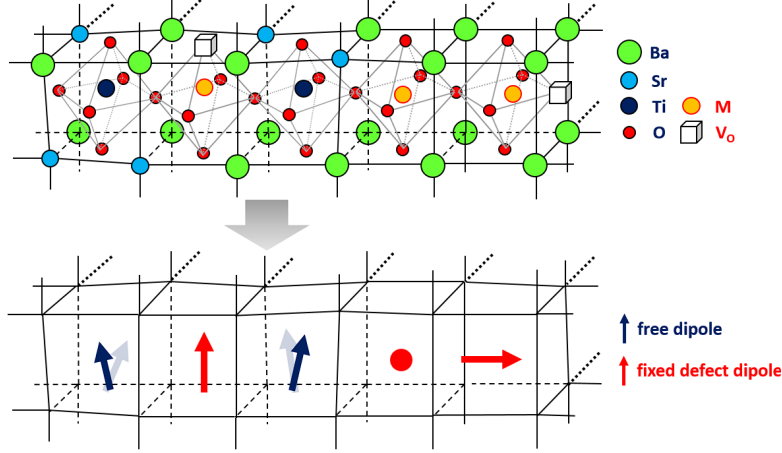


Figure 1: Coarse-graining and modeling of defects: The atomic displacements in all unit cells of $(\text{Ba,Sr})\text{TiO}_3$ are coarse-grained to free dipoles (dark blue arrows) and local strain (optimized internally). If Ti is substituted by another atom (M), the local dipole moment can be reduced. We consider the limiting case of a non-polar cell (red dot). Defect complexes formed by dopant M and an oxygen vacancy (V_O) carry finite dipole moments which switch orders of magnitude slower than the surrounding material and are modeled by frozen-in dipoles (red arrows).

cf. Ref. 30. The other terms in Eq. (1) are the self-energy, V^{self} , the long-range dipole-dipole interaction, V^{dpl} , the short-range harmonic interaction between local modes, V^{short} , the elastic energy from homogeneous and inhomogeneous strains, $V^{elas,homo}$ and $V^{elas,inho}$, the coupling terms between local soft mode and strain, $V^{coup,inho}$ and $V^{coup,inho}$. As the strain is optimized internally, only the dynamics of the dipole moments are explicitly treated in molecular dynamics simulations, using M_{dipole}^* the effective mass of the local soft mode. This coarse-graining is illustrated in Fig. 1.

A supercell with $L_x \times L_y \times L_z = 48 \times 48 \times 48$ u.c. is combined with periodic boundary conditions and the dipoles are initialized with a normal distribution with $\langle u_x \rangle = \langle u_y \rangle = \langle u_z \rangle = 0.00 \text{ \AA}$ and $\langle u_i^2 \rangle - \langle u_i \rangle^2 = 0.03 \text{ \AA}^2$ at 350 K or with $\langle u_x \rangle = \langle u_y \rangle = \langle u_z \rangle = 0.10 \text{ \AA}$ and $\langle u_i^2 \rangle - \langle u_i \rangle^2 = 0.01 \text{ \AA}^2$ at 50 K to perform cooling and heating simulations. For each temperature, we use a time step of $\Delta t = 2$ fs and thermalize the system for 40000 steps in the canonical ensemble using the Nosé-Poincaré thermostat before we calculate the average properties in additional 20000 steps. The final configuration is the input for the next temperature step using $\Delta T = \pm 1$ K. We monitor the absolute values of the macroscopic polarization $|\langle P_i \rangle|$ along direction

i , and the mean of the magnitude of the local polarization $\langle |P_i| \rangle$. Both quantities differ in the presence of domains. Unlike stated otherwise the temperatures of ferroelectric to ferroelectric transitions are identified from the maximum/minimum of strain in the high/low-temperature phase and the paraelectric-ferroelectric transition temperature is determined from the maximal derivative of polarization with respect to temperature.

For chosen equilibrated configurations the field-hysteresis in $\langle 100 \rangle$ -type fields with a magnitude of 150 kV/cm is recorded starting with the negative field direction at the ramping rate of $1.5E16$ V/m/s. Note that the virgin curve for this first poling is not discussed in the following. As shown in Figure 2, each hysteresis loop is characterized by the values of polarization without external bias (P_r^\pm) and in the maximal applied field (P_{max}^\pm), the coercive fields (E_c^\pm), which we determine by the maxima of dP/dE , the widths of the hysteresis loops ($\Delta E_c = |E_c^{(\rightarrow)} - E_c^{(\leftarrow)}|$), the bias fields ($E_{bias} = \frac{1}{N} \sum_i E_c^{(i)}$), the energy density in a unipolar field-cycle which can be reversibly stored ($W_{rec}^\pm = \int_{P_r^\pm}^{P_{max}^\pm} E dP$) and work losses if switching from remanent to saturation polarization ($W_{loss}^\pm = \int_{P_r^\mp}^{P_{max}^\pm} E dP - W_{rec}^\pm$). Furthermore, it is convenient to define the energy storage efficiency η as $\eta = W_{rec}/(W_{rec} + W_{loss})$. Data as well as Jupyter notebooks used for the analysis are available via Zenodo [31] and Gitlab [32].

2.2. Defect dipoles

To depict the range of reasonable defect strengths and concentrations, we first categorize reports on defects from literature. Typical oxygen vacancy and doping concentration are in the range of 0–2 % (i.e. 10^{14} – 10^{21} cm $^{-3}$). [13, 24, 7, 14] It has furthermore been reported that defect dipoles increase [33, 34] or decrease [34] the remanent polarization of the pristine material (P_0). To cover this range, we model defect strengths from 0 to $1.8P_0$ with $P_0 = 28.41$ $\mu\text{C}/\text{cm}^2$ the polarization we find for $(\text{Ba}_{0.7}, \text{Sr}_{0.3})\text{TiO}_3$ at 210 K (tetragonal phase). If not stated otherwise, we use $u = 0.1$ \AA , i.e. $0.9 P_0$ as example.

We take two types of point defects into account. Fig. 1 shows possible microscopic realizations for these scenarios: First, substituents with different radii or electronic structures, e.g., Ce^{4+} or Zr^{4+} on B-site, may prevent the local off-centering in the stoichiometric material and suppress the local dipole moment (illustrates as circle). [9, 6] Second, pairs of a substituent with different valency and an oxygen vacancy may form defect dipoles $M + V$, which

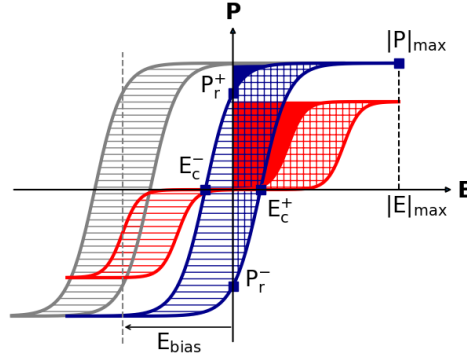


Figure 2: Characteristic field hysteresis representative for the pristine material (dark blue) compared to the pinched hysteresis in the presence of 2D defect agglomerates (red) without remanent polarization ($P_r^\pm = 0$), and the shifted hysteresis with an internal bias field (E_{bias}) induced by defect dipoles collinear with the applied field (gray). E_c^\pm , and P_r^\pm are coercive fields and remanent polarizations for both field directions (E^\pm) and $|P|_{max}$ is the polarization at the maximal field strength E_{max} . Hatched and colored regions illustrate work loss (W_{loss}) and recoverable energy (W_{rec}) in a unipolar field loop.

align with the polarization direction in the tetragonal phase during aging [20] and follow different dynamics than the intrinsic polarization. We approximate these by frozen-in dipoles which are all aligned along one direction, cf. Ref. 18.

To screen the impact of the defect distribution, we focus on defects randomly distributed in the material and clustering in planes and cubes. Fig. 3 collects all defect distributions and concentrations. The largest coupling between defects and surrounding local dipoles is expected along the polarization direction i , as the defects induce a local polarization gradient $\nabla_i P$ and thus a depolarization field. Therefore we define the *active surface area* of a defect configuration as the area of the surface with its normal parallel to a polarization components i , e.g. along the tetragonal axis or along any of the Cartesian directions in the rhombohedral phase, measured in u.c., i.e. unit cells with an area of about 15.6 \AA^2 .

3. Results

3.1. Phase diagrams

We start our analysis with the phase stability without external electrical fields. For defect-free $(\text{Ba}_{0.7}\text{Sr}_{0.3})\text{TiO}_3$, we find transition temperatures

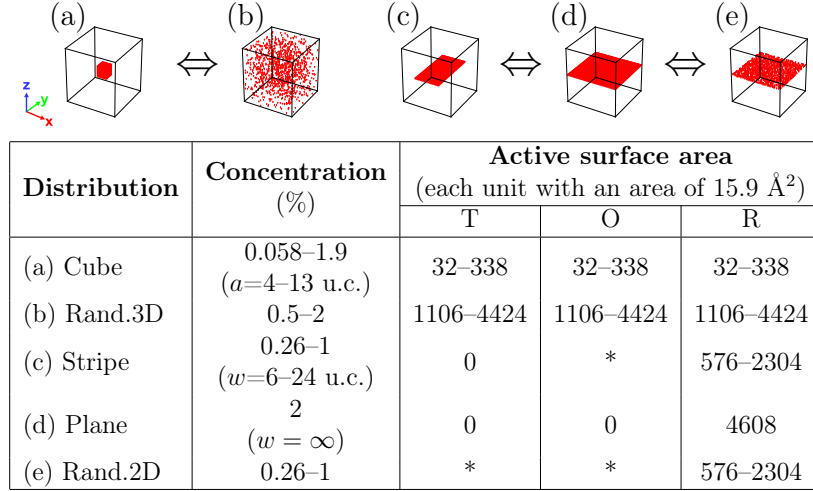


Figure 3: Sampled distributions as well as considered concentrations of defects and their *active surface areas* (table) for: (a) cubic agglomerates, (b) random distribution in 3D, (c)–(e) agglomeration in one plane for (c) compact stripes, (d) full planes and (e) randomly. Thereby a and w are the size and width of the cube and the stripe, respectively. In tetragonal (T), orthorhombic (O) and rhombohedral (R) phases the *active surface area* is defined by the surface of the defects along the polarization direction. Each u.c. contributes an active area of about $(3.9435 \text{ \AA})^2$. As discussed in the text, some 2D configurations have no *effective active area* in T or O phase.

from cubic to tetragonal (T_C^{C-T}) to orthorhombic (T_C^{T-O}), and to rhombohedral (T_C^{O-R}) phases at 293 K, 210 K, and 168 K within the spread of experimental values of about 285–308 K, 217–222 K and 154–172 K, respectively.[35, 36, 37, 38] These transition temperatures are modified with the concentration of non-polar defects, see Fig. 4. Thereby, changing the distribution of defects from random to 3D agglomerates (dashed and solid lines in subfigure (a)) or to 2D agglomerates (subfigure (b)) has a larger impact on the transition temperatures than changing their concentration. First, increasing the concentration of randomly distributed defects induces an approximately linear reduction of T_C^{C-T} of more than 35 K for 2 % defects. Second, agglomeration in 2D mainly reduces T_C^{O-R} , e.g., by 33 K for 1 % of defects and by 92 K for a full plane of defects. Third, cubic agglomerates with up to 2% concentration have a minor impact on all phase transition temperatures. Large agglomerates in 3D and 2D induce a slight increase of T_C^{T-O} , while T_C^{R-O} increases slightly in the presence of large 3D agglomerates or a high concentration of randomly distributed defects. Note that

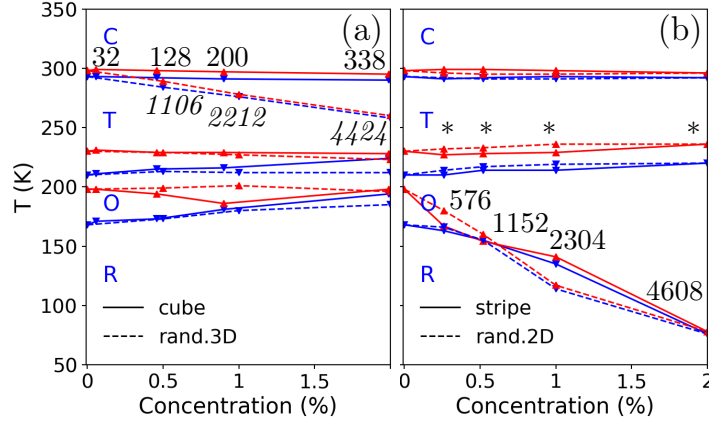


Figure 4: Temperature - defect concentration phase diagrams in the presence of non-polar defects ($|u_D| = 0.0 \text{ \AA}$) for (a) cubic agglomerates (solid lines) and random distribution in 3D (dashed lines) and (b) stripes of defects (solid lines) and random distribution in 2D (dashed lines). Red and blue lines show transition temperatures for heating and cooling, respectively. Numbers give the approximate number of active surface units in (a) T, O (b) and R phases. Note that the defect agglomerates in (b) have no effective *active surface area* for T and O phases as discussed in the text.

the qualitative changes of transition temperatures for randomly distributed defects are in good agreement to the experimental results published for the substitution of Ti by Zr.[7]

Most of these observations can be understood by the change of the *active surface areas* of the defects in the different phases, see Fig. 3. First of all, the *active surface area* along one polarization component impacts T_C^{C-T} . For a given defect concentration, it is maximal for a distribution without direct defect neighbors. Indeed, random distributions induce the largest change of T_C^{C-T} and of macroscopic polarization and strain, see Fig. 5 and cf. Fig. C.12 (a). If the defects cluster in one cube, the *active surface area* is reduced, e.g. by factor of 10 for 1 % defects. Even for 2 % defects in such a cluster, changes of macroscopic polarization and strain are barely visible, cf. Fig. C.13. Both, in case of random distribution and 3D clustering, the *active surface area* does not change if going from T to O or R phase and thus the lower transition temperatures are not too sensitive to the defect concentration. On the other hand, agglomerates in 2D reduce the symmetry of the system and one has to distinguish polarization normal to the defect plane with a large *active surface area* and polarization parallel to the defect plane.

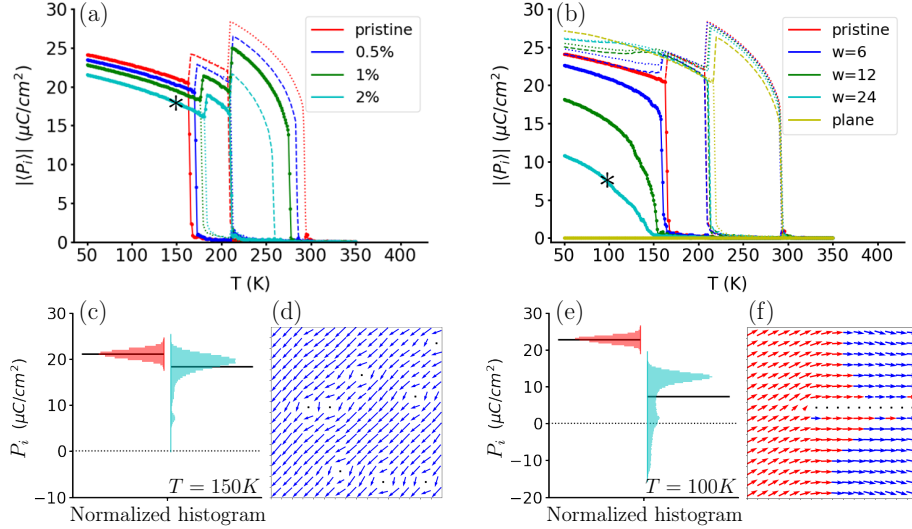


Figure 5: Changes of (a)-(b) polarization components $|\langle P_i \rangle|$, with $i : x, y, z$, in cooling simulations and (c),(e) of dipole histograms, induced by non-polar defects ($|u_D| = 0.0 \text{ \AA}$) for (a),(c),(d) random distribution and (b),(e),(f) stripes in z -planes with varying width (w). For (c) 2 % defects at 150 K and (e) 1 % defects ($w = 24$ u.c.) at 100 K, histograms of local P_z (right) are compared to the pristine reference system (left). (d) and (f) show corresponding time-averages of local dipoles close to the defects color encoded by the sign of P_z .

For T and O phases, the defects stabilize the parallel polarization directions (P_y and $P_x = P_y$) without large active areas and thus T_C^{C-T} and T_C^{T-O} are not modified. Only in the R phase, one polarization component has to point along the normal, is subject to a maximal *active surface area* and T_C^{O-R} is reduced with the defect concentration.

While the main trends of the transition temperatures are thus related to the *active surface areas* of the defects, also their dilution impacts phase stability and dipole configuration. Figure 5 compares the change of macroscopic polarization between defects being (a) randomly distributed and (b) agglomerated in 2D stripes. The underlying histograms of one polarization component in the presence of 2% defects are shown to the right in subfigures (c) and (e), while the histograms to the left correspond to the pristine material at the corresponding temperatures. In case of random distribution, about 4.4 % of the dipoles are reduced (peak around $7.2 \mu\text{C}/\text{cm}^2$). Closer inspection shows that these are mainly nearest neighbors of defects along the polarization direction, cf. Fig. 5 (d). As the defects start to cluster, more

and more defects are reduced along this direction and the coupling between defects and dipoles becomes more long-ranged, see subfigure (f). Already a stripe with $w = 6$ u.c. (i.e. 0.5% defects) induces gradual rotations of dipoles in at least 3 layers next to the agglomerate. Above a critical width of about $w = 12$ u.c., negative domains with a diameter of 8 u.c. form at the defect agglomerate, and for $w = 24$ u.c. the dipoles normal to the defect are modified in the whole system by the formation of domains with R71 walls along [110], cf. Fig. D.15. This increase of the interaction length with the compactness of the defects is only induced along the polarization directions. Thus, while a compact stripe of defects has a finite interface along the x -direction, the induced modifications of P_x are confined to that plane and do not couple to the macroscopic polarization. The effective active area marked as (*) in Fig. 4 is thus zero. Note that also large 3D agglomerates, e.g. $a = 13$ u.c. with an active surface unit of 338 u.c. (cf. Fig. D.15) induce rotations of the dipole in several unit cells and multi-domain structures, in this case for all three polarization directions.

Going from a perfect defect plane to the pristine material is also possible by the dilution of defects on the plane, see dashed lines in Fig. 4 (b). While a multi-domain structure forms for more than 25 % coverage of compact agglomerates, more than 50 % coverage is needed in a diluted plane. Thereby also the change of T_C^{O-R} for small defect concentrations is larger in the former case. On the other hand, the cross-section of the diluted defect plane is larger for a given defect concentration. Once domain walls form, the whole system splits into 2 equidistant R71 stripes and T_C^{O-R} decreases faster for intermediate defect strengths. These changes of the interaction range with the dilution of the defects can be related to the dilution of the depolarization field: On the one hand, the depolarization field by separated defects only couples to the local environment. On the other hand, the fields of dense defects add up, which increases the interaction length and results in the formation of domains above a critical size and density of the agglomerate.

Non-polar defects also modify the character of the transitions and their thermal hysteresis. In the pristine material, all transitions are of first order and we find thermal hysteresis of 5 K, 20 K and 30 K, correspondingly. Generally, the hysteresis is systematically reduced with the concentration of defects, for example to 2 K, 11 K and 11 K for 2 % of randomly distributed non-polar defects. Particularly, the character of the O–R transition can be modified by agglomerated defects, cf. continuous change of polarization for wide agglomerates in Fig. 4. For these configurations, hysteresis closes for

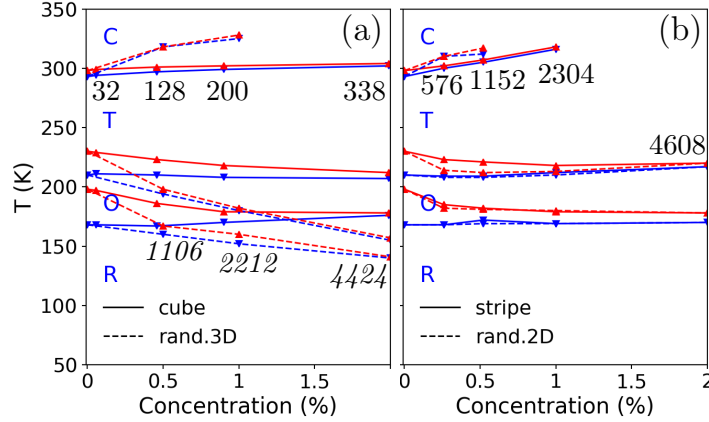


Figure 6: Temperature - defect concentration phase diagrams for polar defects ($|u_D| = 0.1 \text{ \AA} \hat{z}$). Symbols mark transition temperatures for cooling (blue) and heating (red). Note that no C-T transition can be detected for large defect concentrations and magnitudes beyond the critical point. Random ordering (solid lines) and agglomeration (dashed lines) are compared for (a) defects in 3D and (b) defects in a z -plane. Numbers give the approximate number of active surface units in all phases for (a) cube and random distribution (italic) and (b) for stripes.

less than 0.5 % of defects due to the reduction of T_C^{O-R} during heating. Analogously, thermal hysteresis is below our resolution for about 0.5 % and 1 % defects randomly distributed in a plane or clustered in a cube, respectively. This can be understood by the discussed change of the polarization component normal to the agglomerate which induces monoclinic distortions and by domain wall formation in the R phase, as both these modifications may reduce the energy barrier for the transition.[39, 2] Note that a hysteresis of about 15 K remains at the T-O transition even for a full defect plane due to the weak coupling between defects and the polarization parallel to the plane.

In summary, the impact of non-polar defects on the ferroelectric phase diagram is dominated by the effective *active surface area* of the defect configuration and, in case of compact defect agglomerates, depolarization fields modify the domain structure. Similar, but less pronounced changes of the phase stability have to be expected for locally reduced, but finite local dipoles switching by polar off-centering.

Even larger changes of the phase stability are possible in the presence of defect dipoles related to M- V_O complexes with different switching kinetics, as shown exemplary for defects with $|u_D| = 0.1 \text{ (\AA)} \hat{z}$, i.e. $u_x = u_y = 0$, in

Fig. 6. Again, small cubic agglomerates have a minor impact on all phases due to their small *active surface area*. Besides that, the trends differ from the non-polar case. As the polarization of the T phase aligns with the direction of the defect dipoles, all other orderings have similar *active surface area* and T_C^{C-T} increases until a critical point is induced by about 1% defects. Additionally, the transition temperatures under heating for T_C^{T-O} and T_C^{O-R} decrease for small defect concentrations. Already 0.5 % of defects randomly distributed in 2D or 3D thus reduce the thermal hysteresis of the T-O transition to 4 K. Analogous trends have been reported for external fields along $\langle 100 \rangle$. [40, 41, 42] In the tetragonal phase, the defect dipoles thus act as an internal electrical field along the direction of the defect dipoles whose strength can be adjusted with the concentration of the defects. However, in contrast to a homogenous external field also *active surface area* of defects and defect dilution contribute to the coupling between the internal field and the free dipoles. Thus both the change of T_C^{C-T} and the critical defect concentration vary slightly between stripes and random distributions. In case of 2D agglomeration, the effective *active surface area* along x and y is again zero and the transition temperatures to O or R phases under cooling are not sensitive to the defect concentration. On the other hand, randomly distributed defects have an *active surface area* at their non-polar interfaces and thus induce a reduction of T_C^{T-O} of more than 55 K for 2 % defects and also T_C^{O-R} goes down with the defect concentration, see Fig. 6 (a). For 2D agglomerates with, e.g., $|u_D| = 0.1 \text{ (\AA)} \hat{x}$, the defects act similar to non-polar defects, cf. Fig. B.11, with polarization along x and xy in the T and O phases and small changes of the transition temperatures, while T_C^{O-R} decreases by 36 K (1 % of defects) and by 98 K for a full defect plane for the R phase with polarization along z . Comparison between these defects and the non-polar ones shows that the former induces a slight increase of T_C^{C-T} and a reduction of the thermal hysteresis at the T-O transition, while only in the latter case T_C^{T-O} increases slightly for large defect concentrations. All these observations can be related to the small internal fields along x .

The second obvious route to modify the internal field induced by the defect dipoles is tuning of the defect strength. For random defect distribution and cubic agglomerates, the increase of the internal field with defect strength induces the same changes of the phase diagram as the change of the defect concentration, see Fig. 7 (a). However, for 2D agglomerates with polarization along z , where is a cross-over from weak to strong defect dipoles, see Fig. 7 (b). Below $u_z = 0.03 \text{ \AA}$, e.g. about 27% of the saturation polarization

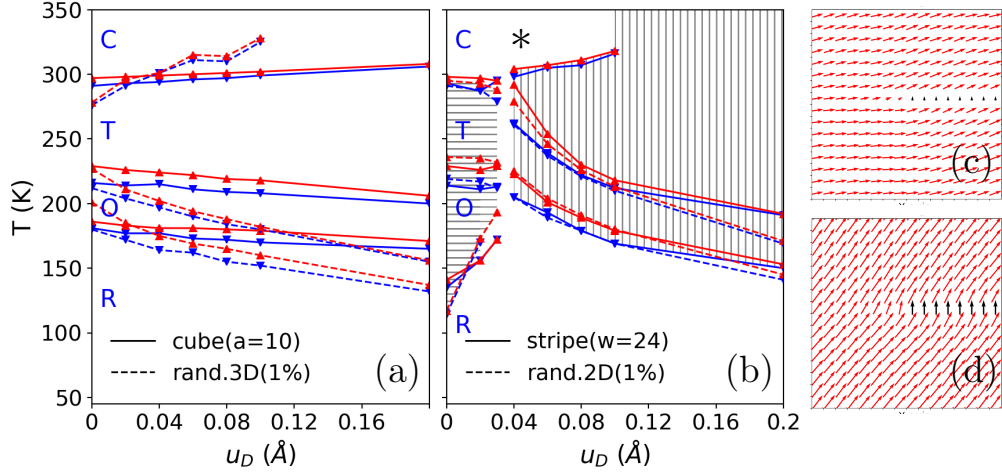


Figure 7: Impact of the strength of 1% defects ($|u_D| \hat{z}$) on the ferroelectric phase diagram. Colors highlight transition temperatures for cooling (blue) and heating (red). Agglomeration (solid lines) and random ordering (dashed lines) are compared for (a) defects in a cube or 3D and (b) defects in one z -plane. In (b) horizontal (=) and vertical (||) hatches mark T and O phases with $P_z = 0$ and $|P_z| > 0$, respectively. (c) and (d) show corresponding time-averaged local dipoles at 200 K for weak defect dipoles ($|u_D| = 0.03 \text{ \AA} \hat{z}$) and strong defect dipoles ($|u_D| = 0.1 \text{ \AA} \hat{z}$), respectively. *Note that beyond 0.04 \AA the sample with 2D random defects is beyond the critical point of the C-T transition.

of the pristine material, the defect dipoles act similar to non-polar defects with polarization in the T and O phases pointing along P_y and $P_y = P_x$, no effective *active surface area* and no change of T_C^{C-T} and T_C^{T-O} . Only in the R phase one polarization component points parallel to the defects and T_C^{O-R} increases with their strength. Thereby the O-R transition becomes continuous, cf. Fig.C.14. For strong defects ($u > 0.03 \text{ \AA}$), the polarization in the T phase point along z and T_C^{C-T} increases up to the critical point, while T_C^{O-R} and T_C^{T-O} decrease with the internal defect field. At the cross-over point, one has to expect that states with P_y and P_z are degenerated which may induce multi-critical points with coexisting C, T and O as well as with coexisting R, O and T phases. The exact cross-over points are beyond our scope, for the chosen resolution of 0.01 \AA , the transition temperatures of the C, T and O as well as of T, O and R phases indeed approach each other.

In summary, in case of 2D agglomeration, non-polar and weak defect dipoles have the same impact on the phase stability while strong defects act as an internal bias field, while defects randomly distributed in 3D induce an

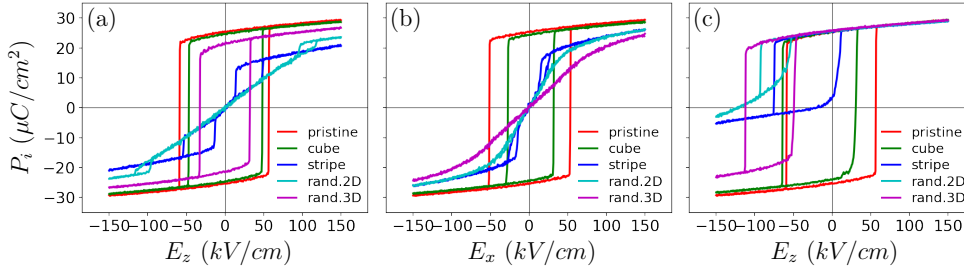


Figure 8: Changes of the field hysteresis at $T = 250$ K if going from the pristine material (red) to systems with different distribution of 1 % defects (green: cube; blue and cyan: stripes and randomly in \hat{z} -planes; purple: randomly) for (a) non-polar defects and (b)–(c) polar defect dipoles ($|u_D| = 0.1 \text{ \AA} \hat{z}$) for the electric field (b) perpendicular (E_x) and (c) collinear (E_z) to the defect dipoles. Only the polarization component P_i along the field direction is shown.

internal bias field for all field strengths.

3.2. P - E Hystereses

How do the different defect configurations affect the field response of the material? As reference, red lines in Fig. 8 show the field hysteresis of the pristine material in the T phase at 250 K. The P – E curve is symmetric, centered at the origin, and has large coercive fields and remanent polarization. Depending on their ordering and strength, defects considerably modify these characteristics, see other colors in Fig. 8 and the corresponding strain–field (σ - E) curves in Fig. E.17. Non-polar or weak defect dipoles, reduce remanent polarization ($|P_r^\pm|$) and particularly the width of the hysteresis loops (ΔE_c) for all orderings while the hysteresis stays symmetric as shown in subfigures (a). Analogous to the phase diagrams, the differences between the configurations are related to the *active surface area* of the defects. The *active surface area* and the impact on the field hysteresis is small for cubic agglomerates and 2D agglomerates with the field applied in the defect plane. In these cases the changes of ΔE_c (and P_r) are below 18 % (3 %) and 20 % (3 %), respectively, cf. Fig. E.16. Larger modifications are induced by randomly ordered defects that have a larger *active surface area*. The largest changes are induced by 2D agglomerates if the field is applied along z . This defect distribution induces depolarization fields and acts as a reversible restoring force on the polarization direction. Thus, the polarization switches between the T phase with P_x and a monoclinic state with $\pm P_z > P_x$, cf. Fig. E.18. The response $P_z(E_z)$ is thus pinched to a double-loop hysteresis. Thereby,

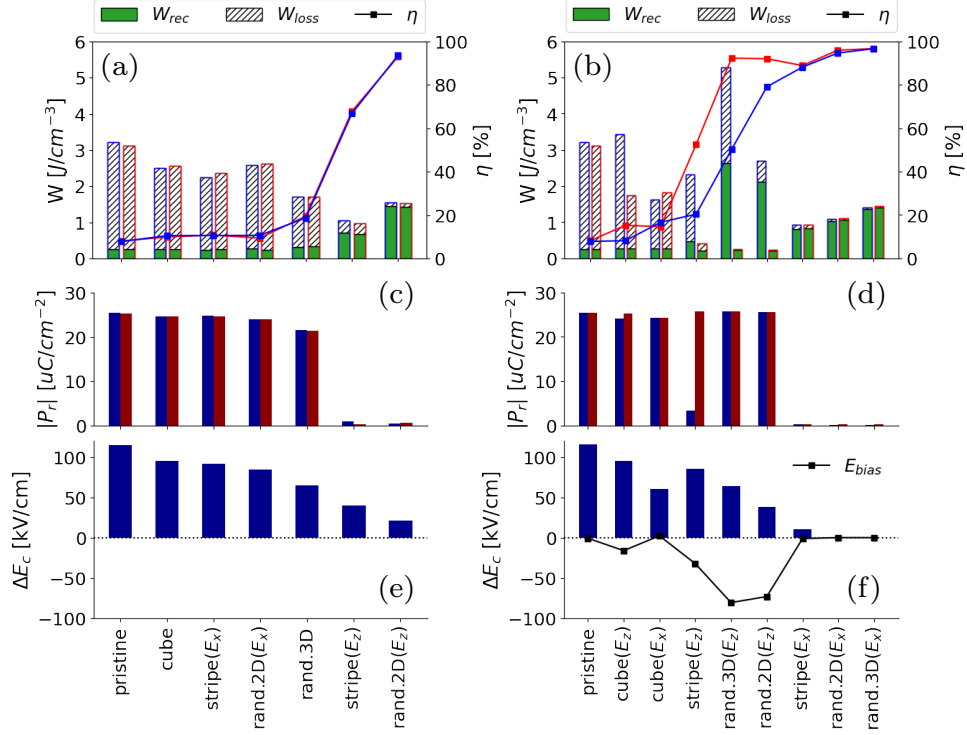


Figure 9: Characteristics of the field hysteresis for 1 % (a,c,e) non-polar and (b,d,f) polar defects ($|u_D| = 0.1 \text{ \AA}\hat{z}$) at $T = 250 \text{ K}$ for $E = 150 \text{ kV/cm}$ sorted by efficiency. In (a)–(b) W_{rec} (green) and W_{loss} (gray hatched) and the efficiency η (black dots, right axes), in (c)–(d) the remanent polarization $|P_r|$ and in (e)–(f) the width of the hysteresis (ΔE_c) and the bias field E_{bias} for different defect distributions are compared to the pristine material. Red and blue correspond to positive and negative field directions which differ for the collinear alignment of defects and the external field (E_z).

for the chosen defect concentration of 1%, the randomly distributed defects in one plane impact the surrounding dipoles more than stripes, cf. discussion on Fig. 5, and stabilize a reversible linear change of P_z with the field for more than $\pm 96 \text{ kV/cm}$.

As shown in subfigure (b), strong defect dipoles along z furthermore induce full pinching of the hysteresis for a perpendicular field along x . In this case, internal and external fields compete with each other for all orderings. For both 2D agglomerates and a random distribution of defects, the remanent polarization along the field direction is zero and the strain response is maximized, cf. Fig. E.17 and Fig. E.18. There is no hysteresis for randomly distributed defects and a double hysteresis loop is induced in field ranges

of less than 10 kV/cm by compact stripes. Strong defect dipoles collinear to the field, shown in subfigure (c), reduce the width of the field hysteresis, e.g. by about 28 % for the cubic agglomerates and by about 45 % for random ordering in 3D. Furthermore, these defects act as internal bias fields and shift the center of the hysteresis to negative E_z . Thereby larger changes are induced in E_c^+ , i.e. parallel to the defect direction, and E_c^+ is shifted to negative field directions for random defect distributions. For the cube, with its small *active surface area* only this positive coercive field is reduced. Increasing the *active surface area*, not only E_c^+ shifts further, but also P_r^- is reduced. These trends can be understood by pinned dipoles. Already for the cube, its neighbors along the polarization direction do not switch for the chosen field strength and thus act as nucleation centers for the macroscopic switching towards the positive polarization direction lowering the coercive field. Going from cube to random in 3D and finally to agglomeration in 2D, the interaction length between defects and surrounding dipoles and thus the pinned volume increase, cf. Fig. E.19. Additionally, the increase of $|E_c^-|$ induced by the internal bias field, increases from stripe to random in plane to random in 3D. This again shows that the *active surface area* governs the main trends of polarization and phase stability, while the subtle details also depend on the compactness or dilution of defects.

Figure 9 compares the characteristics of the hysteresis loops for all defect configurations. For the pristine material, a work loss of about 3 J/cm^{-3} is dissipated if the polarization switches from P_r^- to the saturation polarization P_{max}^x and vice versa for negative field directions, while the recoverable work as well as reversible changes of polarization and strain without switching are negligible, in qualitative agreement with previous reports.[43] On the one hand, non-polar or weak defects in most configurations induce a small reduction of the loss only. The efficiency η is thus approximately constant and increases slightly for random defects. On the other hand, large efficiencies are possible for the double loop hysteresis found for 2D ordering. Thereby, the smallest hysteresis in case of defects randomly distributed in one plane allows for an efficiency of about 94 %. Analogously, pinched hysteresis with reduced losses and maximal ΔP and η are stabilized by strong defects along z in a field along x as long as the *active surface area* is not reduced by clustering in 3D. Maximal recoverable energy and efficiency of 1.07 J/cm^{-3} and 96 % are possible for defects randomly distributed in the sample. Finally, for strong defects and fields along z , one has to distinguish between positive and negative field directions. In the former case shown in red, no polar-

ization switching can be induced during unipolar field loops for randomly distributed defects and thus the used definition of loss and efficiency would predict optimal configurations. However, this is not relevant as the possible recoverable energy as well as changes of P and strain are negligible. In case of the negative field shown in blue, maximal values of W_{rec} and a moderate efficiency are possible due to the shifted and reduced hysteresis for random defect distributions.

In summary, the field characteristics depend strongly on the defect arrangement and the relative direction of the field. Weak defects induce the largest modification of the hysteresis if they agglomerate in 2D, while the pinching of the hysteresis for strong defect dipoles perpendicular to the field is maximal for randomly oriented dipoles. Finally, strong defects parallel to the field induce the largest shift of hysteresis for random distribution, while 2D agglomerates induce the largest asymmetry.

4. Conclusion

While it is commonly accepted that point defects and defect complexes in ferroelectric perovskites modify ferroelectric phase diagrams and field hysteresis, the impact of defect distribution and agglomeration is so far under-represented. In this study, we have used *ab initio* based simulation to close this knowledge gap.

We have analyzed a range of defect concentrations and strengths of defect dipoles. Thereby we found a cross-over between non-polar or weak defect dipoles, which mainly induce local depolarization fields, and strong defect dipoles larger than about 30% of the saturation polarization of the tetragonal phase, which induce internal electrical fields. Both types of defects reduce thermal hysteresis and coercive field and affect the phase diagram by less than 1% defect. We have shown that, both for phase stability and field hysteresis, the spatial distribution of defects and their agglomeration are thereby more important than their exact concentration or strength. Specifically, depolarization and internal fields are associated with the *active surface area* of the defect configuration. Thus, randomly distributed defects have e.g. the largest impact on the paraelectric to ferroelectric phase transition. Agglomeration or clustering reduces this *active surface area* and thus the impact of the defects on the material. Thus, large changes of functional properties are to be expected for the formation or decomposition of defect clusters with time. Most interesting are defect agglomerates in two dimensions, which reduce the

symmetry of the system. In this case, independent of the defect type, i.e. the strength of the defect dipole, particular polarization directions are favored by the defects. Thus phase stability and field hysteresis depend on the relative direction of defect agglomerate and external field. Pinched hysteresis loops and large recoverable stored energy are possible for one direction, while the defects are rather invisible in the other direction. The control of defect dipole strengths (e.g., by using different dopants), agglomeration (e.g., by ion bombardment), as well as the prevention of ion migration (e.g., by heat treatment and interfaces) are thus promising routes to tap the full potential of defect engineering in ferroelectric materials. One promising route to tailor material properties by defects may thus be the design of 2-dimensional defect-rich areas. Furthermore, it was interesting to further explore if there are atomistic realizations of defect dipoles close to the cross-over strength, which could be utilized to introduce multi-critical points in the phase diagram.

Acknowledgments

Funding: This work was supported by the German research foundation (DFG) GR 4792/2. We thank Prof. Dr. Markus Stricker for his helpful comments and fruitful discussions.

Declaration of generative AI in scientific writing

During the preparation of this work, the authors used DeepL and Grammarly for wording suggestions and checking of language. After using these tools, we reviewed and edited the content as needed and take full responsibility for the content of the publication.

References

- [1] R. W. Whatmore, Y.-M. You, R.-G. Xiong, C.-B. Eom, 100 years of ferroelectricity—A celebration, *APL Mater.* 9 (7) (2021) 070401. doi: 10.1063/5.0059208.
URL <https://aip.scitation.org/doi/full/10.1063/5.0059208>
- [2] A. Grünebohm, M. Marathe, R. Khachatryan, R. Schiedung, D. C. Lupascu, V. V. Shvartsman, Interplay of domain structure and phase transitions: Theory, experiment and functionality, *J. Phys.: Condens.*

Matter 34 (7) (2021) 073002. doi:10.1088/1361-648X/ac3607.
URL <https://doi.org/10.1088/1361-648x/ac3607>

- [3] V. Veerapandiyan, F. Benes, T. Gindel, M. Deluca, Strategies to Improve the Energy Storage Properties of Perovskite Lead-Free Relaxor Ferroelectrics: A Review, *Materials* 13 (24) (2020) 5742. doi:10.3390/ma13245742.
URL <https://www.mdpi.com/1996-1944/13/24/5742>
- [4] R. Khosla, S. K. Sharma, Integration of Ferroelectric Materials: An Ultimate Solution for Next-Generation Computing and Storage Devices, *ACS Appl. Electron. Mater.* 3 (7) (2021) 2862–2897. doi:10.1021/acsaelm.0c00851.
URL <https://doi.org/10.1021/acsaelm.0c00851>
- [5] V. F. Michel, T. Esswein, N. A. Spaldin, Interplay between ferroelectricity and metallicity in BaTiO₃, *J. Mater. Chem. C* 9 (27) (2021) 8640–8649. doi:10.1039/D1TC01868J.
URL <https://pubs.rsc.org/en/content/articlelanding/2021/tc/d1tc01868j>
- [6] V. Veerapandiyan, M. N. Popov, F. Mayer, J. Spitaler, S. Svirskas, V. Kalendra, J. Lins, G. Canu, M. T. Buscaglia, M. Pasciak, J. Banys, P. B. Groszewicz, V. Buscaglia, J. Hlinka, M. Deluca, Origin of Relaxor Behavior in Barium-Titanate-Based Lead-Free Perovskites, *Adv. Electron. Mater.* 8 (2) (2022) 2100812. doi:10.1002/aelm.202100812.
URL <https://onlinelibrary.wiley.com/doi/abs/10.1002/aelm.202100812>
- [7] M. Acosta, N. Novak, V. Rojas, S. Patel, R. Vaish, J. Koruza, G. A. Rossetti, J. Rödel, BaTiO₃-based piezoelectrics: Fundamentals, current status, and perspectives, *Appl. Phys. Rev.* 4 (4) (2017) 041305. doi:10.1063/1.4990046.
URL <https://aip.scitation.org/doi/10.1063/1.4990046>
- [8] A. Dimou, A. Biswas, A. Gruenebohm, Ab initio based study on atomic ordering in (Ba, Sr)TiO₃ (Aug. 2023). arXiv:2308.13263, doi:10.48550/arXiv.2308.13263.
URL <http://arxiv.org/abs/2308.13263>

- [9] N. A. Hill, Why Are There so Few Magnetic Ferroelectrics?, *J. Phys. Chem. B* 104 (29) (2000) 6694–6709. doi:10.1021/jp000114x.
URL <https://doi.org/10.1021/jp000114x>
- [10] Y.-B. Ma, C. Molin, V. V. Shvartsman, S. Gebhardt, D. C. Lupascu, K. Albe, B.-X. Xu, State transition and electrocaloric effect of $\text{BaZr}_x\text{Ti}_{1-x}\text{O}_3$: Simulation and experiment, *Journal of Applied Physics* 121 (2) (2017) 024103. doi:10.1063/1.4973574.
URL <https://doi.org/10.1063/1.4973574>
- [11] Y. W. Li, J. F. Scott, D. N. Fang, F. X. Li, 90-degree polarization switching in BaTiO_3 crystals without domain wall motion, *Appl. Phys. Lett.* 103 (23) (2013) 232901. doi:10.1063/1.4832784.
URL <https://aip.scitation.org/doi/10.1063/1.4832784>
- [12] H.-Y. Huang, M. Wu, L.-J. Qiao, The behaviour of 180° polarization switching in BaTiO_3 from first principles calculations, *Comp. Mater. Sci.* 82 (2014) 1–4. doi:10.1016/j.commatsci.2013.09.013.
URL <https://www.sciencedirect.com/science/article/pii/S0927025613005375>
- [13] Y. A. Genenko, J. Glaum, M. J. Hoffmann, K. Albe, Mechanisms of aging and fatigue in ferroelectrics, *Mater. Sci. Eng. B* 192 (2015) 52–82. doi:10.1016/j.mseb.2014.10.003.
URL <https://www.sciencedirect.com/science/article/pii/S0921510714002189>
- [14] M. Krupska-Klimczak, P. Gwizd, I. Jankowska-Sumara, D. Sitko, P. Jeleń, An Overview of Some Nonpiezoelectric Properties of BaTiO_3 Ceramics Doped by Eu Ions, *Materials* 15 (15) (2022) 5363. doi:10.3390/ma15155363.
URL <https://www.mdpi.com/1996-1944/15/15/5363>
- [15] Z. Li, J. Yu, S. Hao, P.-E. Janolin, Enhancing properties of lead-free ferroelectric BaTiO_3 through doping, *J. Eur. Ceram. Soc.* 42 (12) (2022) 4693–4701. doi:10.1016/j.jeurceramsoc.2022.05.023.
URL <https://www.sciencedirect.com/science/article/pii/S0955221922003673>

- [16] X. Ren, Large electric-field-induced strain in ferroelectric crystals by point-defect-mediated reversible domain switching, *Nat. Mater.* 3 (2) (2004) 91–94. doi:10.1038/nmat1051.
URL <https://www.nature.com/articles/nmat1051>
- [17] J. Li, J. Lv, D. Zhang, L. Zhang, X. Hao, M. Wu, B.-X. Xu, M. Otonicar, T. Lookman, B. Dkhil, X. Lou, Doping-induced Polar Defects Improve the Electrocaloric Performance of $\text{Ba}_{0.9}\text{Sr}_{0.1}\text{Hf}_{0.1}\text{Ti}_{0.9}\text{O}_3$, *Phys. Rev. Appl.* 16 (1) (2021) 014033. doi:10.1103/PhysRevApplied.16.014033.
URL <https://link.aps.org/doi/10.1103/PhysRevApplied.16.014033>
- [18] A. Grünebohm, T. Nishimatsu, Influence of defects on ferroelectric and electrocaloric properties of BaTiO_3 , *Phys. Rev. B* 93 (13) (2016) 134101. doi:10.1103/PhysRevB.93.134101.
URL <https://link.aps.org/doi/10.1103/PhysRevB.93.134101>
- [19] L. Zhang, E. Erdem, X. Ren, R.-A. Eichel, Reorientation of $(\text{Mn}_{\text{Ti}}'' - \text{V}_{\text{O}}^{\bullet\bullet})^{\times}$ defect dipoles in acceptor-modified BaTiO_3 single crystals: An electron paramagnetic resonance study, *Appl. Phys. Lett.* 93 (20) (2008) 202901. doi:10.1063/1.3006327.
URL <https://aip.scitation.org/doi/10.1063/1.3006327>
- [20] P. Erhart, P. Träskelin, K. Albe, Formation and switching of defect dipoles in acceptor-doped lead titanate: A kinetic model based on first-principles calculations, *Phys. Rev. B* 88 (2) (2013) 024107. doi:10.1103/PhysRevB.88.024107.
URL <https://link.aps.org/doi/10.1103/PhysRevB.88.024107>
- [21] Z. Zhang, Z. Wen, T. Li, Z. Wang, Z. Liu, X. Liao, S. Ke, L. Shu, Flexoelectric aging effect in ferroelectric materials, *J. Appl. Phys.* 133 (5) (2023) 054102. doi:10.1063/5.0134531.
URL <https://aip.scitation.org/doi/full/10.1063/5.0134531>
- [22] C. Verdier, D. C. Lupascu, H. von Seggern, J. Rödel, Effect of thermal annealing on switching dynamics of fatigued bulk lead zirconate titanate, *Appl. Phys. Lett.* 85 (15) (2004) 3211–3213. doi:10.1063/1.1801679.
URL <https://doi.org/10.1063/1.1801679>

- [23] D. C. Lupascu, Agglomeration and Microstructural Effects, in: D. C. Lupascu (Ed.), *Fatigue in Ferroelectric Ceramics and Related Issues*, Springer Series in Materials Science, Springer, Berlin, Heidelberg, 2004, pp. 63–79. doi:10.1007/978-3-662-07189-2_3.
URL https://doi.org/10.1007/978-3-662-07189-2_3
- [24] S. Saremi, R. Xu, F. I. Allen, J. Maher, J. C. Agar, R. Gao, P. Hosemann, L. W. Martin, Local control of defects and switching properties in ferroelectric thin films, *Phys. Rev. Mater.* 2 (8) (2018) 084414. doi:10.1103/PhysRevMaterials.2.084414.
URL <https://link.aps.org/doi/10.1103/PhysRevMaterials.2.084414>
- [25] T. Suzuki, M. Ueno, Y. Nishi, M. Fujimoto, Dislocation Loop Formation in Nonstoichiometric $(\text{Ba,Ca})\text{TiO}_3$ and BaTiO_3 Ceramics, *J. Am. Ceram. Soc.* 84 (1) (2001) 200–206. doi:10.1111/j.1151-2916.2001.tb00631.x.
URL <https://ceramics.onlinelibrary.wiley.com/doi/abs/10.1111/j.1151-2916.2001.tb00631.x>
- [26] S. M. Yang, T. H. Kim, J.-G. Yoon, T. W. Noh, Nanoscale Observation of Time-Dependent Domain Wall Pinning as the Origin of Polarization Fatigue, *Adv. Funct. Mater.* 22 (11) (2012) 2310–2317. doi:10.1002/adfm.201102685.
URL <https://onlinelibrary.wiley.com/doi/abs/10.1002/adfm.201102685>
- [27] D. Akbarian, D. E. Yilmaz, Y. Cao, P. Ganesh, I. Dabo, J. Munro, R. V. Ginhoven, A. C. T. van Duin, Understanding the influence of defects and surface chemistry on ferroelectric switching: A ReaxFF investigation of BaTiO_3 , *Phys. Chem. Chem. Phys.* 21 (33) (2019) 18240–18249. doi:10.1039/C9CP02955A.
URL <https://pubs.rsc.org/en/content/articlelanding/2019/cp/c9cp02955a>
- [28] K. K. Adepalli, J. Yang, J. Maier, H. L. Tuller, B. Yildiz, Tunable Oxygen Diffusion and Electronic Conduction in SrTiO_3 by Dislocation-Induced Space Charge Fields, *Advanced Functional Materials* 27 (22) (2017) 1700243. doi:10.1002/adfm.201700243.

URL <https://onlinelibrary.wiley.com/doi/abs/10.1002/adfm.201700243>

- [29] W. Zhong, D. Vanderbilt, K. M. Rabe, First-principles theory of ferroelectric phase transitions for perovskites: The case of BaTiO₃, *Phys. Rev. B* 52 (9) (1995) 6301–6312. doi:10.1103/PhysRevB.52.6301. URL <https://link.aps.org/doi/10.1103/PhysRevB.52.6301>
- [30] T. Nishimatsu, A. Grünebohm, U. V. Waghmare, M. Kubo, Molecular Dynamics Simulations of Chemically Disordered Ferroelectric (Ba,Sr)TiO₃ with a Semi-Empirical Effective Hamiltonian, *J. Phys. Soc. Jpn.* 85 (11) (2016) 114714. doi:10.7566/JPSJ.85.114714. URL <https://journals.jps.jp/doi/10.7566/JPSJ.85.114714>
- [31] S.-H. Teng, Impact of defects on the phase diagram and field response of ferroelectric (Ba,Sr)TiO₃ (Mar. 2024). doi:10.5281/zenodo.8418579. URL <https://zenodo.org/records/8418579>
- [32] S.-H. Teng, Sheng-Han Teng / p1-defect_study · GitLab (Mar. 2024). URL https://gitlab.ruhr-uni-bochum.de/tengssh/p1-defect_study
- [33] S. Liu, R. E. Cohen, Multiscale simulations of defect dipole-enhanced electromechanical coupling at dilute defect concentrations, *Appl. Phys. Lett.* 111 (8) (2017) 082903. doi:10.1063/1.4989670. URL <https://aip.scitation.org/doi/10.1063/1.4989670>
- [34] R. Machado, A. Di Loreto, A. Frattini, M. Sepiarsky, M. G. Stachiotti, Site occupancy effects of Mg impurities in BaTiO₃, *J. Alloy. Compd.* 809 (2019) 151847. doi:10.1016/j.jallcom.2019.151847. URL <https://www.sciencedirect.com/science/article/pii/S0925838819330865>
- [35] Y. Zhou, D. Yang, G. Jiang, Effect of Yttrium Doping on Microstructure and Temperature Resistance Characteristics of Barium Strontium Titanate Ferroelectric Ceramics, in: 2022 IEEE International Conference on High Voltage Engineering and Applications (ICHVE), 2022, pp. 1–4. doi:10.1109/ICHVE53725.2022.9961754.
- [36] B. Vigneshwaran, P. Kuppusami, S. Ajithkumar, H. Sreemoolanadhan, Study of low temperature-dependent structural, dielectric, and

- ferroelectric properties of $\text{Ba}_x\text{Sr}_{(1-x)}\text{TiO}_3$ ($x = 0.5, 0.6, 0.7$) ceramics, *J Mater Sci: Mater Electron* 31 (13) (2020) 10446–10459. doi:10.1007/s10854-020-03593-3.
URL <https://doi.org/10.1007/s10854-020-03593-3>
- [37] J. W. Liou, B. S. Chiou, Dielectric characteristics of doped $\text{Ba}_{1-x}\text{Sr}_x\text{TiO}_3$ at the paraelectric state, *Mater. Chem. Phys.* 51 (1) (1997) 59–63. doi:10.1016/S0254-0584(97)80267-2.
URL <https://www.sciencedirect.com/science/article/pii/S0254058497802672>
- [38] V. V. Lemanov, E. P. Smirnova, P. P. Syrnikov, E. A. Tarakanov, Phase transitions and glasslike behavior in $\text{Sr}_{1-x}\text{Ba}_x\text{TiO}_3$, *Phys. Rev. B* 54 (5) (1996) 3151–3157. doi:10.1103/PhysRevB.54.3151.
URL <https://link.aps.org/doi/10.1103/PhysRevB.54.3151>
- [39] B. Noheda, D. E. Cox, G. Shirane, S.-E. Park, L. E. Cross, Z. Zhong, Polarization Rotation via a Monoclinic Phase in the Piezoelectric 92% $\text{PbZn}_{1/3}\text{Nb}_{2/3}\text{O}_3$ -8% PbTiO_3 , *Phys. Rev. Lett.* 86 (17) (2001) 3891–3894. doi:10.1103/PhysRevLett.86.3891.
URL <https://link.aps.org/doi/10.1103/PhysRevLett.86.3891>
- [40] M. Marathe, A. Grünebohm, T. Nishimatsu, P. Entel, C. Ederer, First-principles-based calculation of the electrocaloric effect in BaTiO_3 : A comparison of direct and indirect methods, *Phys. Rev. B* 93 (5) (2016) 054110. doi:10.1103/PhysRevB.93.054110.
URL <https://link.aps.org/doi/10.1103/PhysRevB.93.054110>
- [41] M. Marathe, D. Renggli, M. Sanlialp, M. O. Karabasov, V. V. Shvartsman, D. C. Lupascu, A. Grünebohm, C. Ederer, Electrocaloric effect in BaTiO_3 at all three ferroelectric transitions: Anisotropy and inverse caloric effects, *Phys. Rev. B* 96 (1) (2017) 014102. doi:10.1103/PhysRevB.96.014102.
URL <https://link.aps.org/doi/10.1103/PhysRevB.96.014102>
- [42] N. Novak, R. Pirc, Z. Kutnjak, Impact of critical point on piezoelectric and electrocaloric response in barium titanate, *Phys. Rev. B* 87 (10) (2013) 104102. doi:10.1103/PhysRevB.87.104102.
URL <https://link.aps.org/doi/10.1103/PhysRevB.87.104102>

- [43] B. Luo, X. Wang, E. Tian, L. Wu, L. Li, First-principles effective Hamiltonian simulation of ABO_3 -type perovskite ferroelectrics for energy storage application, *J. Appl. Phys.* 120 (7) (2016) 074106. doi: 10.1063/1.4961204.
URL <https://aip.scitation.org/doi/10.1063/1.4961204>

Appendix A. Pristine material

The phase diagram of $\text{Ba}_{0.7}\text{Sr}_{0.3}\text{TiO}_3$ as found for the pristine case (without defect dipoles) is shown in Fig. A.10. Thereby, subfigures (a) and (b) show the change of the macroscopic polarization components and of the lattice constants, respectively.

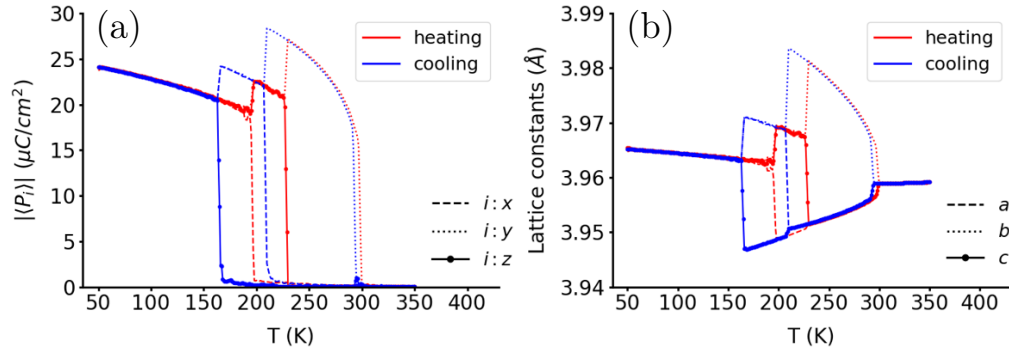


Figure A.10: Temperature dependence of (a) polarization components ($|\langle P_i \rangle|$, where $i : x, y, z$), and (b) lattice constants (a, b, c correspond to the length along x, y, z) of $\text{Ba}_{0.7}\text{Sr}_{0.3}\text{TiO}_3$ without defects. Colors encode cooling (blue) and heating (red) simulations.

Appendix B. Phase diagrams

Figure B.11 compares phase diagrams in the presence of (a) polar defect dipoles in the plane ($|u_D| = 0.1 \text{ \AA}\hat{x}$) and (b) non-polar defects ($|u_D| = 0 \text{ \AA}$) for 2D agglomerates (solid lines) and random distribution in 2D (dashed lines).

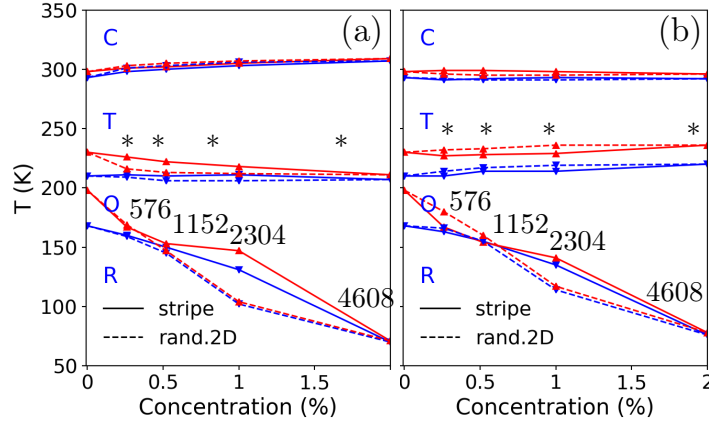


Figure B.11: Temperature - defect concentration phase diagrams in the presence of (a) polar defect dipoles ($|u_D| = 0.1 \text{ \AA}\hat{x}$) and (b) non-polar defects ($|u_D| = 0.0 \text{ \AA}$) for stripes of defects (solid lines) and random distribution in 2D (dashed lines). Red and blue lines show transition temperatures for heating and cooling, respectively. Numbers give the approximate number of active surface units in R phases. Note that the defect agglomerates have no effective *active surface area* for T and O phases as discussed in the text.

Appendix C. Macroscopic changes of polarization and strain by non-polar defects

Figure C.12 (a) and (b) show the change of macroscopic strain components (σ_{ii} with $i = x, y, z$) for random distribution in 3D and 2D agglomerates with varying concentration or width. Figure C.13 (a) and (b) show the change in macroscopic polarization and strain for cubic agglomerates. Figure C.14 (a) and (b) show the impact of defect dipole strength on the change of macroscopic polarization for 1 % defects of 2D random distribution and 2D agglomerate.

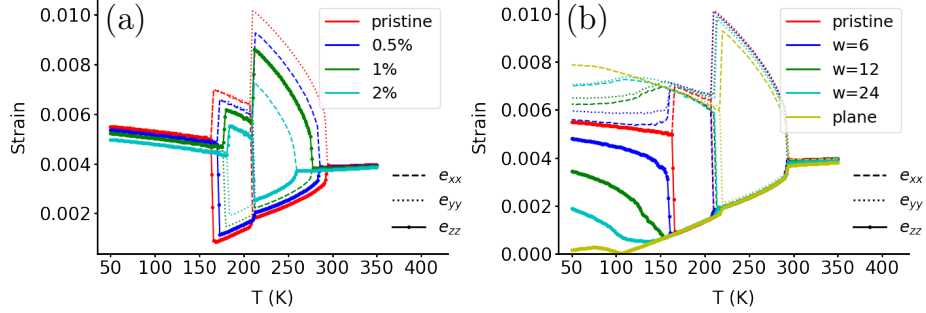


Figure C.12: Changes of strain components σ_{ii} , with $i : x, y, z$, in cooling simulations induced by non-polar defects ($|u_D| = 0.0 \text{ \AA}$) for (a) random distribution and (b) stripes in z -planes with varying width (w).

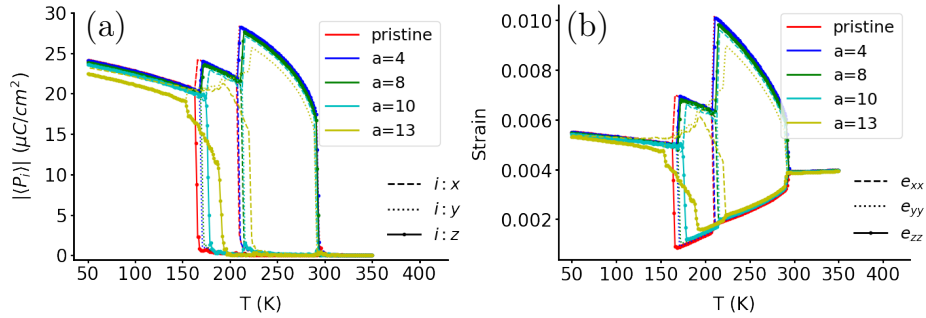


Figure C.13: Changes of (a) polarization components $|P_i|$ and (b) strain components σ_{ii} , with $i : x, y, z$, in cooling simulations induced by non-polar defects ($|u_D| = 0.0 \text{ \AA}$) with varying length (a) of cube. Note that for the cube with $a = 13$ u.c., depolarization fields induce multidomains, resulting in a continuous O-R phase transition.

Appendix D. Microscopic changes of polarization by defects

Figure D.15 (a) and (b) show the microscopic polarization for a 2D agglomerate of $w = 12$ u.c. and a cubic agglomerate of $a = 13$ u.c., showing the formation of R71 domain walls above/below the agglomerates.

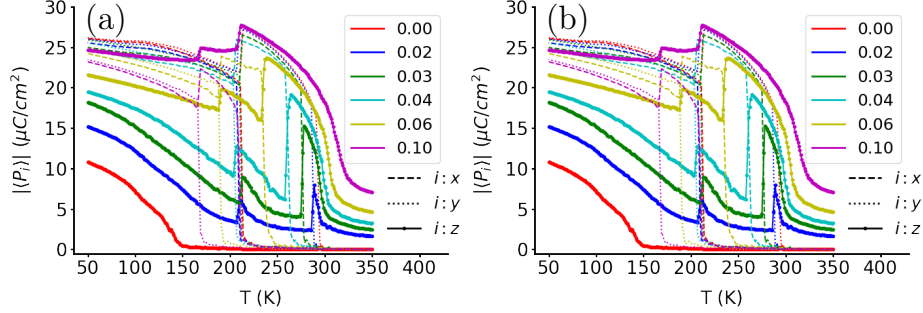


Figure C.14: Impact of the strength of 1 % defects ($|u_D| \hat{z}$) on the changes of polarization components $|\langle P_i \rangle|$, with $i : x, y, z$, in cooling simulations for (a) random distribution and (b) stripes. Colors encode the strength of the defect dipoles from 0.00 (red), 0.02 (blue), 0.03 (green), 0.04 (light blue), 0.06 (light green) to 0.10 (purple).

Appendix E. Field hysteresis and snapshots

Figure E.16 (a) and (b) show the change in macroscopic polarization and strain for the pristine to system with non-polar defects in cubic, 2D agglomerate and 2D random distributions with the bipolar field E_x applied. Figure E.17 (a), (b) and (c) show the strain–field (σ - E) curves for non-polar defects with the electric field E_z and polar defects with the electric field E_x or E_z applied. Figure E.18 (a) and (b) show all 3 polarization components for non-polar defects with bipolar field E_z applied, while Fig. E.18 (a) and (b) are for polar defects ($|u_D| = 0.1 \text{ \AA} \hat{z}$) with the bipolar electric field E_x perpendicular to the defect dipoles. Figure E.19 shows snapshots of systems with 1 % defects of cubic agglomerate, 3D random distribution, 2D agglomerate and 2D random distribution at $E_z = -150 \text{ kV/cm}$, showing pinned domains near defects that could act as nucleation centers for the macroscopic switching towards the positive polarization direction.

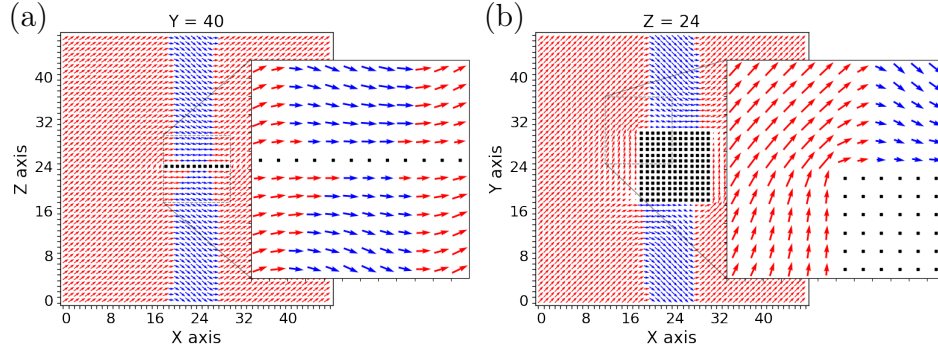


Figure D.15: Cross section of time-averaged local dipoles in the presence of (a) a 2D agglomerate with 0.5 % ($w = 12$ u.c.) non-polar defects at 100 K (R phase) and (b) a cube with 2 % ($a = 13$ u.c.) non-polar defects at 100 K, showing R71 domain walls. Colors indicate the sign of P_z s.

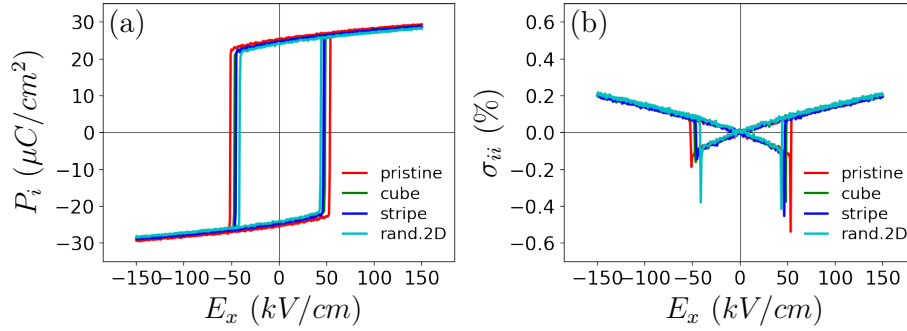


Figure E.16: Changes of the field hysteresis at $T = 250$ K if going from the pristine material (red) to systems with different distribution of 1 % defects (green: cube; blue and cyan: stripes and randomly in \hat{z} -planes) for non-polar defects for the electric field perpendicular (E_x) to the defect dipoles. Only the polarization component P_i and strain component σ_{ii} along the field direction are shown.

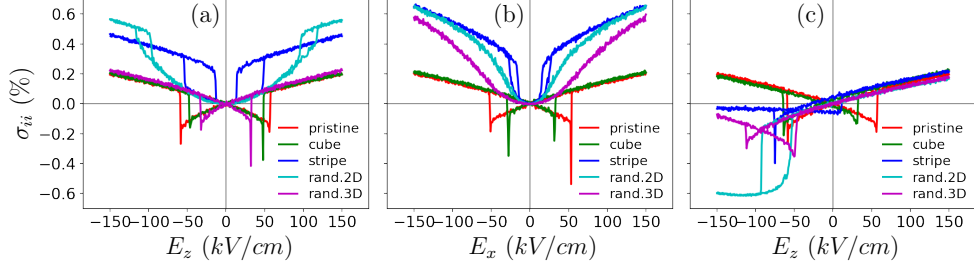


Figure E.17: Changes of the field hysteresis at $T = 250$ K if going from the pristine material (red) to systems with different distribution of 1 % defects (green: cube; blue and cyan: stripes and randomly in \hat{z} -planes; purple: randomly) for (a) non-polar defects and (b)–(c) polar defect dipoles ($|u_D| = 0.1 \text{ \AA}\hat{z}$) for the electric field (b) perpendicular (E_x) and (c) collinear (E_z) to the defect dipoles. Only the diagonal strain component σ_{ii} along the field direction is shown.

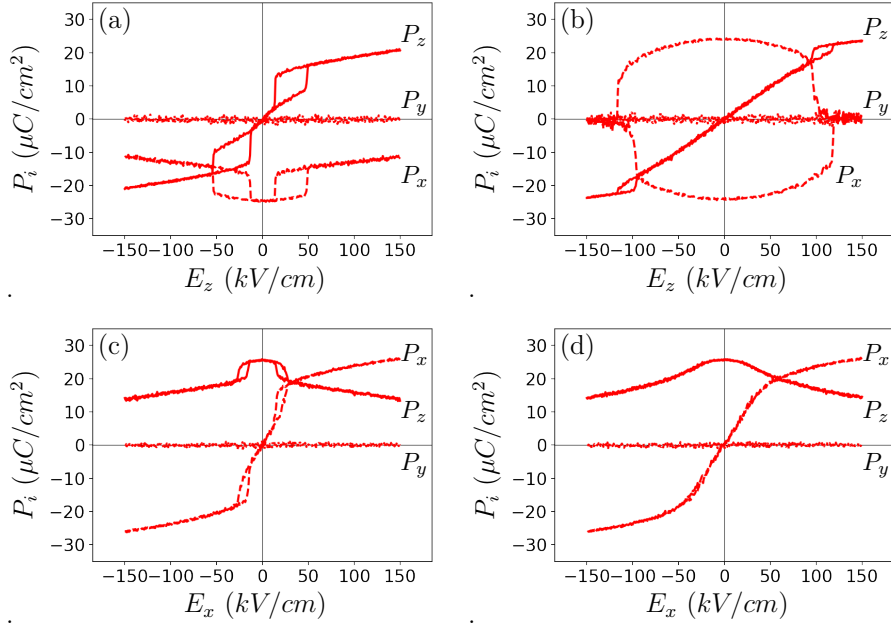


Figure E.18: Field dependence of polarization component P_i with $i = x, y, z$ at $T = 250$ K with 1 % defects for (a,c) stripes and (b,d) randomly in one plane for (a,b) non-polar defects and (c,d) polar defects with ($|u_D| = 0.1 \text{ \AA}\hat{z}$) for the electric field (a,b) along the z or (c,d) perpendicular (E_x) to the defect dipoles.

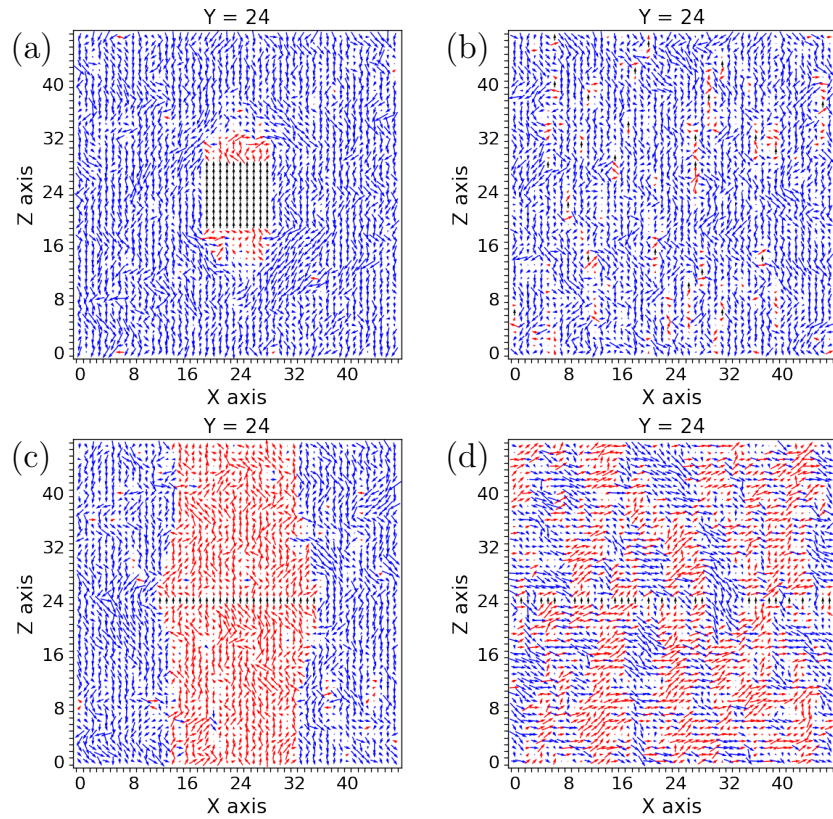


Figure E.19: Snapshots of dipoles at 250 K for 1 % defects ($|u_D| = 0.1 \text{ \AA} \hat{z}$) in (a) cubic agglomerate of $a = 10$ u.c., (b) 3D random, (c) 2D agglomerate of $w = 24$ u.c. and (d) 2D random in a plane with the applied field $-150 \text{ kV/cm } \hat{z}$. Colors indicate the sign of P_z s. Note that all these snapshots are not time-averaged and are thus noisy.